RESEARCH ARTICLE

Spectral-Spatial Features Extraction of Hyperspectral Remote Sensing Oil Spill Imagery Based on Convolutional Neural Networks

TAO HU[1,2], JING YUAN[1], XIAODONG WANG[1], CHANGXIANG YAN[1,3], AND XUEPING JU[1]

[1]Changchun Institute of Optics, Fine Mechanics and Physics, Chinese Academy of Sciences, Changchun 130033, China
[2]University of Chinese Academy of Sciences, Beijing 100049, China
[3]Center of Materials Science and Optoelectronics Engineering, University of Chinese Academy of Sciences, Beijing 100049, China

Corresponding author: Changxiang Yan (yancx0128@126.com)

ABSTRACT Marine oil spills accidents has caused a large amount of crude oil to leak into the marine environment and threaten marine ecological environment. Hyperspectral remote sensing images (HRSI) technology can quickly and accurately identify oil film of different thickness on marine surface. In order to overcome the traditional spectrum analysis method and space extraction method of long time sampling, calculation, analysis and other shortcomings. On account of the advantages of the spectral and spatial information in the field of HRSI classification, a spectral-spatial features extraction (SSFE) method based convolutional neural networks (CNNs) was proposed to analyse oil spills. In this way, one and two dimensional models based on convolutional neural networks (1D-CNN,2D-CNN) have been introduced as the spectral and spatial features extractor. When extracting spatial features, double-two convolution layers are connected to increasing nonlinearity and reduce the number of parameters. Furthermore, in order to address overfitting and imbalance samples, L2 regularization, class_weight and drouput is added to classes data modeling. More importantly, principal component analysis (PCA) is applied to data dimension reduction, 1D-CNN and 2D-CNN is combined into a unified model further extract the joint spatial-spectral features. To evaluate the effectiveness of the proposed approach, three hyperspectral datasets were utilized, including: University of Pavia dataset, oil spill area 1, oil spill area 2. Experimental results reveal that the proposed method have a very satisfactory performance and better distinguish oil spills.

INDEX TERMS Marine oil spills, hyperspectral remote sensing images (HRSI), convolutional neural networks (CNNs), spectral-spatial features extraction (SSFE).

I. INTRODUCTION

Oil spills accidents are generally characterized as causing enormous economic losses and unbalance of the marine ecosystem due to human activities [1]. Pipeline leakage and marine transportation accidents generally leads to the massive oil spills incidents around the world. Offshore oil tankers release a significant amount of oil. The threat to aquatic ecosystems is much greater than other sources of pollution [2], [3]. Thus, it is important to detect floating oil slicks accurately.

Hyperspectral remote sensing images (HRSI) contain several hundreds of spectral data channels of the same view and have the characteristics of high spectral resolution and a lot of data and have been used in many domains [4]–[8]. Jinghui *et al.* [9] have proposed a joint collaborative

The associate editor coordinating the review of this manuscript and approving it for publication was Wenming Cao.

representation by using the locally adaptive dictionary [9]. It cuts down the negative influence of unprofitable pixels and increases HRSI classification performance. Fang *et al.* [10] have used the local covariance matrix to encode the relationship between different spectral bands. In traditional classification methods, such as random forests (RF) [11], decision tree [12], neural network (NN) [13] and support vector machine (SVM) [14]. These methods only consider the spectral characteristics of the HRSI information, ignored the spatial information of hyperspectral image classification in the important role of loss of hyperspectral image spatial structure information, resulting in the classification accuracy is not high.

The number of studies related to oil spills that employed deep learning models has increased since 2017. These models were applied to a variety of different tasks, such as oil spill detection and identification [15], [16], image classification based on patch [17]–[19], and image segmentation and description [20]–[26]. Relying on the neural network framework, deep learning (dl) models can vary based on their structure, elements, and assignments, which can make up convolution layers, pooling layers, fully connected layers, activation functions, storage locations, gates, decoder, and others [27]. Commonly used dl models include convolutional neural networks (CNNs), autoencoder (AE), recurrent neural network (RNN), deep belief network (DBN) and generative adversarial network (GAN) [28].

Recently, convolutional neural network (CNN) is one of the most representative network models on computer vision fields and tasks [29], [30]. There are three common hyperspectral classification methods based on CNN, among which 1D-CNN extracts spectral information [31], 2D-CNN extracts spatial information, and 3D-CNN [32] is usually composed of a convolution kernel of three dimensions, which can not only take into account the texture spatial features of two-dimensional plane, but also extract the characteristics of different spectrum channels. Şakaci and Urhan [33] used 3D-CNN to construct an end-to-end deep learning network, and the network achieved higher precision than 2D-CNN without any pre-processing or post-processing. Leng *et al.* [34] extracted space-spectrum features of local areas by 3D-CNN, which improved the classification accuracy. Although 3D-CNN performs well in space-spectrum information fusion [35], compared with 1D-CNN and 2DCNN, network computing cost and parameters quantity increase, which is not conducive to the training of large-scale models [31].

In view of the above problems, scholars put forward a variety of solutions. Roy *et al.* [36] proposed a fusion algorithm of 3D-2D CNN, which arranged multi-band spectral images into data cubes similar to playing cards in spectral order. 3D-CNN was first used to extract space-spectrum joint information in three-dimensional space, and 2D-CNN was used to further learn more abstract spatial information in each spectral image. The new 3D-2D CNN based on attention mechanism proposed by Zhang *et al.* [37] and the dual-flow
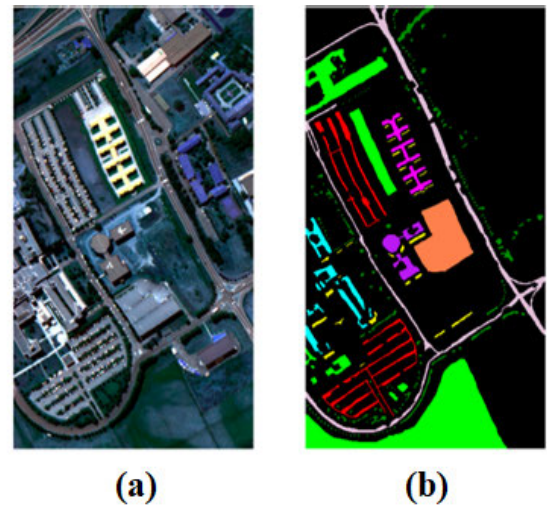
FIGURE 1. University of Pavia dataset. (a) False color image (bands 10, 27, and 46) (b) Ground-truth map.

CNN designed by Han *et al.* [38] also further refined the spatial features. In short, 2D-CNN cannot extract good spectral distinguishing features, 3D-CNN has low computational efficiency and poor performance in hyperspectral classification with similar texture features [36]. However, research on oil spills classification based on CNNs with hyperspectral images is still in its insufficient. Most CNNs models focus only on spectral or spatial features.

The main reason for HRSI have intensity spatial coherence and high spectral resolution, the fusion of spectral and spatial information is supposed to promote classification accuracy. In this study, a fresh spectral-spatial feature extraction (SSFE) method based CNNs is proposed for the HRSI classification. In the method, 1D-CNN is used to extract spectral features, 2D-CNN is served as to extract spatial features. Finally, spectral-spatial features are fused based on the CNNs model. Experiment results demonstrate that the proposed method can were effectively used to detect marine oil spills. Section II describes datasets used in this experiment and the proposed SSFE method for oil spills analysis in detail. Section III is given to the experimental results and comparative analysis to fully verify the effectiveness of SSFIN. Discussions and conclusions are conducted in Section IV and Section V.

II. MATERIALS AND METHODS
A. HYPERSPECTRAL IMAGE DATASETS
University of Pavia dataset was collected by the Reflective Optics System Imaging Spectrometer (ROSIS) over the city of Pavia, Italy, with 610 pixels $\times$ 340 pixels and 115 bands in the range of 0.43 μm–0.86 μm. After removing water absorption and low SNR bands, 103 bands were left for the analysis. It contains 9 ground truth objects. Shown in Figure 1 are the RGB false-color image and nine ground truth classes of Pavia University.

In April 2010, BP's deep water horizon (dwh) oil rig off northern Mexico exploded and began leaking oil into the
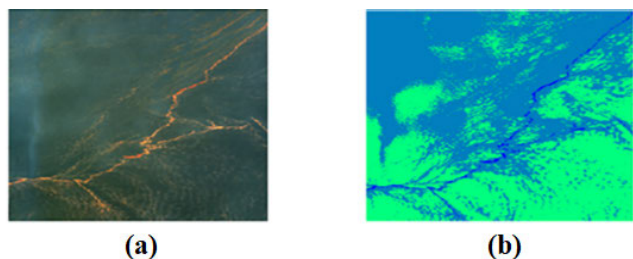
FIGURE 2. Oil spill area 1. (a) False color composite (bands12, 20, and 29) (b) three categories.
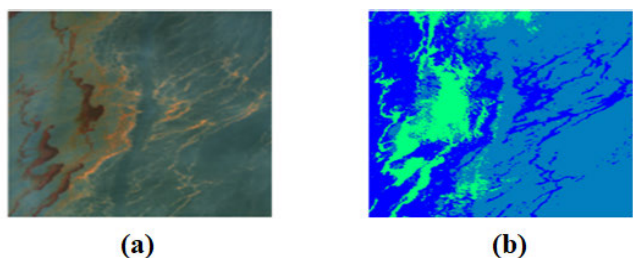

FIGURE 3. Oil spill area 2. (a) False color composite (bands12, 20, and 29) (b) three categories.

Marine environment. Between 66,000 and 120,000 gallons of oil are spilling every day at the heart of the accident. In this paper, airborne AVIRIS (Airborne Visible Infrared Imaging Spectrometer) hyperspectral images of the oil spill were used as experimental areas [39], [40].

The experimental data obtained from Jet Propulsion Laboratory (JPL) official website. The image of experiment oil area 1 and the image of experiment oil area 2 was taken on May 17, 2010, with the flight number f100517t01p00r11. The spatial resolution of data in two experimental areas is 7.6 m. The wavelengths range from 365 nm to 2466 nm in a total of 192 bands, noise bands caused by moisture absorption in the original data have been removed. The software used in this study cannot process such a large area of data at one time, so the sample area is selected for the experiment. The size of oil spill area 1 is 526 pixels × 685 pixels and the coverage area is 20.75 km^2. The size of oil spill area 2 is 425 pixels × 540 pixels and the coverage area is 13.17 km^2. Figure 2 and 3 are the RGB false-color image and three categories of oil area 1 and oil area 2.

B. DATA PREPROCESSING
Radiometric calibration and atmospheric correction were performed on hyperspectral original data. Radiometric correction is the process of removing these noises, such as: reflection of objects, reflection of adjacent ground objects, atmospheric influence, the image contains noise etc. The purpose of atmospheric correction is to eliminate the influence of atmospheric and illumination factors on surface reflectance and obtain real physical model parameters, such as: surface reflectance, emissivity and surface temperature. Radiometric correction was carried out by the data provider

and atmospheric correction needs to be done by individuals. As to obtain surface reflectance values, atmospheric calibration is necessary. The data is the calibrated radiance (emissivity) data, in units is of μW/(cm^2 × nm × sr). Finally, the atmospheric correction were dealt with using the Fast Line-of-sight Atmospheric Analysis of Hypercubes (FLAASH) module using ENVI software. In the FLAASH model, the atmospheric model is based on the data acquisition time and the dimension of the study area, so the American standard atmospheric model is selected. The aerosol model selects maritime according to the actual situation of the study area.

C. FRAMEWORK OF PROPOSED METHOD
1) BASIC FRAMEWORK OF CNN
In general, the basic CNN framework is consisted by input layer, convolution layer, pooling layer, fully connected layer [41]. Through convolution operation, more complex image features can be extracted and signal noise can be reduced. In the pooling layer, redundant information is removed, reduce the size of the model and accelerate the calculation speed, which the number of compressed data and parameters while improve the robustness of extracted features. The full connection layer maps the "distributed feature representation" learned to the sample tag space. At the same time, the nonlinear expression ability of the model is increased.

Convolutional layer is a relatively crucial part of CNN framework, convolution can be used for image edge detection, sharpening, blurring, etc. Each channel of the convolutional layer can be formulated as [42]:

$$a_i^m = h\left(\sum a_j^{m-1} * k_{ij}^m + b_i^m\right). \quad (1)$$

where $i \in N_j$, N_j is a selection set of feature maps, a_i^m denotes the activation value of output feature graph j in layer m, k_{ij}^m is the convolutional kernel, b_i^m is bias. "∗" denotes the convolutional operator. $h(\cdot)$ is rectified activation function.

Common pooling methods are mean pooling max pooling overlapping def-pooling local contrast normalization def-pooling. One of the most commonly used is maximum pooling. The pooling process can be expressed as:

$$a^m = h(\alpha^m a^{m-1} + b^m) \quad (2)$$

where α^m, the weight factor that connects adjacent, a^{m-1} is the characteristic vector of. b^m is the bias vector. In order to preserve more texture information, this paper choose the maximum pooling.

After convolution and maxpooling, a series of feature images are obtained, and the input of the multilayer perceptron is a vector. Furthermore, for purpose of strengthen the nonlinear mapping capability of the network and restrict the magnitude of the network in the meantime, it is necessary to take out the pixels in these feature graphs in turn, arrange them into a vector, and then access to a fully connected layer. Finally, the last layer of convolutional neural network usually adopts fully connected layers and softmax layers with
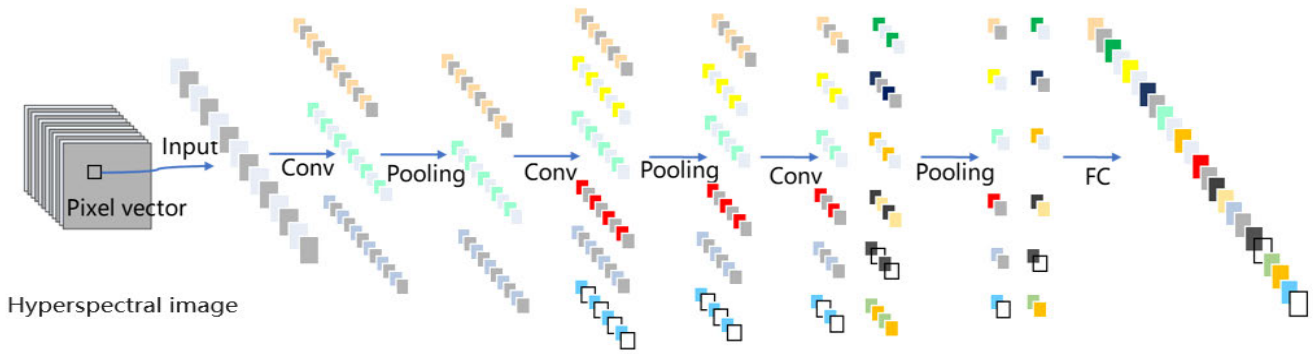
FIGURE 4. The framework of 1D-CNN with spectral features for HRSI classification.

strong nonlinear classification power as classifier to predict the labels.

2) SPECTRAL FEATURE EXTRACTION BASED 1D-CNN FRAMEWORK

In this section, 1D-CNN method is presented here to considering only spectral information of seawater and oil spills. For spectral feature extraction, which includes two procedures: features extraction and classification. Assuming N is the number of HRSI spectral bands, $x = [x_1, x_2, \cdots, x_{N-1}]$, x_n represent the nth pixel, each pixel vector of hyperspectral image is adopted as the input data. The output of the method is the label of the pixel vector. It consists of three convolutional three maxpooling layers and an fully connected layer. The proposed method is shown in Figure 4. To make the best of the shallow and deep features, two consecutive convolution layers are concatenated in sequence, which results in more feature channels. The two convolutional layers are followed by a maxpooling layer with a size of 3 pixels and a stride of 3 pixels, After several layers of convolution and maxpooling, the input pixel vector can be stretched into a one-dimensional feature vector. Finally, we use fully connected layer and softmax classifier to obtain spectral feature $R_{spe}^n(x_n)$.

3) SPATIAL FEATURE EXTRACTION BASED 2D-CNN FRAMEWORK

2D-CNN is adopted here to extract the spatial features. It contains several convolutional layers, pooling layers and a fully connected layer. To remove the redundancy of hyperspectral data, the traditional principal component analysis (PCA) is firstly applied over the dimensionality of hyperspectral oil spill data. Assuming the three-dimensional hyperspectral data cube can be expressed as $S \in C^{M \times N \times B}$, where S is the hyperspectral data input, M and N represent the width and height of data, and B represents the bands number. Through PCA treatment, the number of spectral bands from B to L, that means there are fewer channels. For convenience, after the PCA reduced data cube are denoted as $I \in C^{M \times N \times L}$, where I is the recomposed input after PCA, L is the number of spectral bands after PCA. We choose r × r neighborhoods of

a current pixel as the input to the 2D-CNN model. According to the spatial resolution of the image, a small kernel can be selected to run convolution and 2 × 2 kernel stride of 2 pixels for pooling. Finally, we use fully connected layer and softmax classifier to obtain spatial feature $R_{spa}^n(x_n)$. The framework is shown in Figure 5.

4) SPECTRAL–SPATIAL FEATURES EXTRACTION FRAMEWORK

1D-CNN and 2D-CNN are concatenated in sequence, then fed together into the fully connected layer and linked to the softmax layer. To obtain the joint spectral-spatial feature, $R_{spe}^n(x_n)$ and $R_{spa}^n(x_n)$ are merged and fed together into the fully connected layer. $H^m(x_n)$ is given by:

$$H^{m+1}(x_n) = g\left(K^{m+1} \cdot \left(R_{spe}^n(x_n) \oplus R_{spa}^n(x_n)\right) + b^{m+1}\right)$$

(3)

where K^{m+1} and b^{m+1} represent the weight factors and bias of the fully connected layer, "$\oplus$" denotes the concatenating operator, and $g(\cdot)$ is the ReLU activation function. $H^{m+1}(x_n)$ to predict the prediction of probability distribution of each class. The framework is shown in Figure 6.

To enhance the robustness of the model, adding L2 regularization term with the value of 1×10^{-4} to the objective function and limit the number of weight parameters, The dropout method prevents complex co-adaptations [43]. Batch Normalization normalizes each convolutional layer of the neural network, which results in a more even distribution of data. As a result, all data does not lead to neuron activation, or all data does not lead to neuron activation. Meanwhile, The variable learning rate technique was used to improve the performance of the model, that is keep changing the learning rate, observing the convergence curve of the value of the objective function and the accuracy of the training set until reducing the learning rate does not affect the decline of the objective function or the accuracy of the verification set.

The Adam optimizer [44] is further employed to update the parameters during the process of gradient descent. The Adam optimizer has the advantages of straightforward implementation, high computational efficiency, and low memory requirements. It uses momentum and an adaptive learning rate
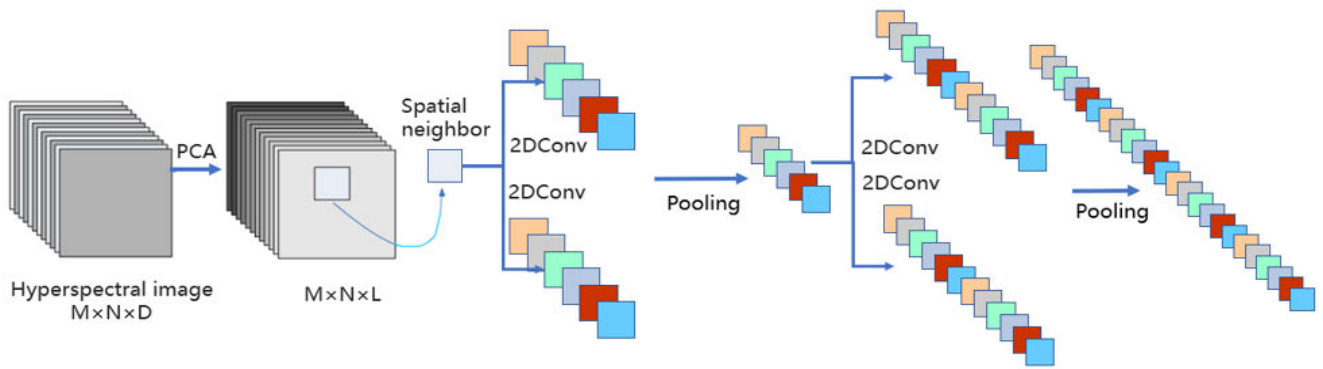
FIGURE 5. The framework of 2D-CNN with spectral features for HRSI classification.
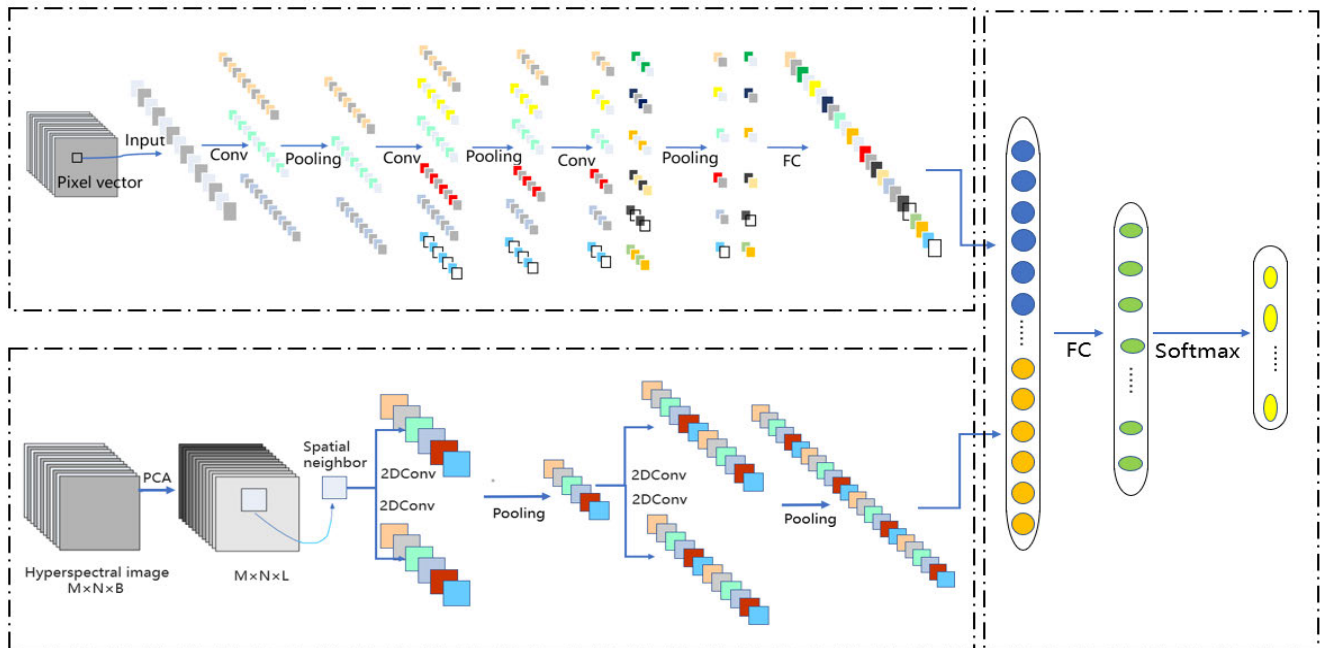

FIGURE 6. The framework of the proposed spectral-spatial features extraction.

to accelerate the convergence rate, thereby quickly getting the predicted results. A more detailed parameter description of the designed SSFE-based HRSI is shown in Table 1. Table 1 shows the structures of the proposed SSFE for the three datasets, "Pavia University", oil spill area 1, oil spill area 2. C, P, F represent the convolution layers, maxpooling layers, fully connected layers, the number after the letter represents the frame number. L2 regularization with a weight decay penalty of 1×10^{-4} has been applied to each convolutional layer. In this paper, to prevent network overfitting and underfitting, class_weight assign a weight to each class in the training or test samples, if the number of class in this categories is large, its weight is low; otherwise, its weight is high. In order to accelerate model convergence speed and train good results, adding the Glorot Uniform and the bias to every convolution operation. Beyond that, the ReLU activation function is added in model and reduced parameter interdependence.

III. EXPERIMENTS AND ANALYSIS
A. DATA PARTITION AND ENVIRONMENT CONFIGURATION

In the experiments, three HRSIs were applied to the experiments, namely Pavia University, oil spill area 1, and oil spill area 2. In all datasets, 10% and 90% of the labeled data are randomly divided to testing and training samples. The function of the training set is in the training process of training error gradient descent, learning, trainable weight parameters. The function of test set is to measure the performance and evaluate the generalization capability of the final model. Tables 2–4 list the sample numbers in the above training and testing groups. All experiments are conducted in Python, and were constructed using Keras and TensorFlow. An Lenovo 15ITL 2021 with NVIDIA GeForce MX450 graphical processing unit (GPU) and 16 GB RAM were used. Under constant trial and error, We find the best optimal learning rate of 0.0005. In view of the size of training set and the

TABLE 1. Architectures of the proposed network structure on three datasets.

	Input	Layer	Filter(number)	Stride	Padding	Droupout
		C1	10(20)	1	Same	No
		P1	3	3	No	No
		C1	10(40)	1	Same	No
1D-CNN	1×103/ 1×192	P1	3	3	No	No
		C1	10(80)	1	Same	No
		P1	3	3	No	No
		F1	-	-	-	No
		C2	(3,3)(30)	1	Same	No
		C2	(3,3)(30)	1	Same	No
		P2	(2,2)	(2,2)	No	No
2D-CNN	1×25×25/ 1×17×17	C2	(3,3)(30)	1	Same	No
		C2	(3,3)(30)	1	Same	No
		P2	(2,2)	(2,2)	No	No
		F2	-	-	-	No
		Concat1	-	-	-	0.25
spectral-spatial		F3	256	-	-	No
		Softmax	3/9	-	-	No

TABLE 2. Land cover types,training and testing numbers on the university of pavia dataset.

No.	Class	Train	Test
1	Asphalt	5958	673
2	Meadows	16944	1705
3	Gravel	1832	267
4	Trees	2701	363
5	Metal Sheets	1189	156
6	Bare Soil	4260	769
7	Bitumen	1131	199
8	Bricks	3393	289
9	Shadows	832	115
Total		38240	4536

TABLE 3. Three categories, training and testing numbers on the oil spill area 1.

No.	Class	Train	Test
1	Thin oil	139724	16434
2	Discontinuous oil	181805	19601
3	Emulsified oil	2476	270
Total		324005	36305

TABLE 4. Three categories, training and testing numbers on the oil spill area 2.

No.	Class	Train	Test
1	Thin oil	30979	3281
2	Discontinuous oil	111890	12813
3	Emulsified oil	63411	7126
Total		206280	23220

GPU platform we used, the batch size is set as 100 for Pavia University dataset and oil spill datasets, respectively. The maximum number of iterations is set to be 100 epochs. All experiments were operated at least 20 times.

B. CLASSIFICATION RESULTS AND ANALYSIS

In order to achieve better classification effect, we used 10% of the testing samples to come up with the optimum parameters of feature extraction (FE) methods. Tables 5–7 show

TABLE 5. Compare the classification results of different methods on the Pavia University dataset.

No.	Class	Adaboost	RF	KNN	SVM	Lenet-5	1D-CNN	2D-CNN	CNN$_{spe+spa}$
1	Asphalt	86.70	91.48	86.18	70.01	97.42	94.89	97.42	98.32
2	Meadows	91.92	98.03	95.93	78.68	99.14	96.54	99.78	98.48
3	Gravel	67.58	72.69	69.47	81.21	85.28	78.67	94.34	97.79
4	Trees	83.57	89.48	79.11	97.85	93.76	95.88	95.55	99.71
5	Metal Sheets	98.27	99.43	98.82	99.62	98.68	100.00	99.63	100.00
6	Bare Soil	74.32	71.48	53.57	86.59	93.90	84.54	99.63	99.28
7	Bitumen	74.55	81.00	78.36	95.58	85.96	81.77	90.79	99.42
8	Bricks	79.03	88.68	79.60	83.84	95.02	91.31	96.78	98.52
9	Shadows	99.21	99.87	99.89	100.00	97.18	98.94	92.74	100.00
	OA	86.00	90.78	84.96	81.82	96.37	92.71	96.65	99.59
	(%)	±0.18	±0.34	±0.09	±0.35	±0.12	±0.26	±0.28	±0.08
	Kappa	85.43	87.62	79.59	76.83	95.19	90.32	95.57	99.46
	(%)	±0.20	±0.27	±0.06	±0.25	±0.07	±0.30	±0.27	±0.04
	Test.Time(s)	115.71	128.13	234.15	159.13	277.36	194.98	257.17	298.64
	Train.Time(s)	17.68	12.45	127.89	64.21	52.49	104.71	160.53	143.66

that the CNN-based FE methods always provide the best performances of overall accuracy (OA) and Kappa coefficient (Kappa) for all three data sets [45]. Here, OA represents the percentage of the total number of test sets that are predicted correctly; and in practical problems, the number of various samples is not balanced, and the model classification tends to favor the large category and abandon the small category. In this paper, it is necessary to conduct a induced test on the number of Kappa lines, whose range is $-1 \sim 1$, and usually falls between $0 \sim 1$. The closer the value is to 1, the higher the consistency is. Confuse matrix and receiver operating characteristic (ROC) curve are used to judge the quality of classification and test results. The classification precision values are concluded in the form of mean ± standard deviation from a statistical point of view, which is used to judge the stability of network and the volatility of data. Concerning both of the two abovementioned indicators, the F1-score, also known as balanced F Score, is defined as the harmonic average of accuracy and recall rate [46]. It is of particular importance for unbalanced classes.

In this set of experiments, the proposed SSFE was compared with RF, SVM, KNN, Adaboost [47], LeNet-5 [48], 1DCNN [49], and 2DCNN [50]. Table 5 shows the accuracies related to the OA and Kappa for different methods for the Pavia University data set while maintaining the minimum standard deviation. Compared with 1D-CNN methods, 2D-CNN methods take full advantage of strong spatial correlation and generate better classification effect. The proposed CNN$_{spe+spa}$ avoided the oversmoothing phenomenon and the edge information of different kinds of ground objects has been fully extracted. classification precision of two classes reach 100% among the classes of different ground objects.

Figure 7 show the visualization of classification results of models of Pavia University data set under different methods, It can be seen from the figure that if only spectral features are used, the ''Bare soil'' category may be more affected by

noise and therefore exhibit small patches. On the contrary, the addition of spatial features can obviously improve the unsmooth phenomenon in the classification map. In conclusion, the proposed method effectively avoids the shortcomings of using only spectral and spatial features, and achieves better visualization results.

Figure 8 and Figure 9 shows the visualization of oil spill detection results from the proposed model on two oil spill datasets. As shown in these figures, the method proposed here presents classification results of high purity from the perspective of visual effect. As expected, the oil spill detection results obtained by using spectral features alone, SVM or Lenet-5 for instance, are more susceptible to noise such as solar flares, leading to misclassification. For example, several speckled areas of thin oil are misclassified as a discontinuous oil in the upper left corner of oil spill area 1. After adding spatial information, the situation affected by noise can be greatly reduced. However, the small patches phenomenon may occur, for instance detection area above emulsified oil film area by 2D-CNN, as presented in Figure 9f. The proposed SSFE algorithm, integrating both spectral information and spatial information, not only relieved the occurrence of misclassification phenomenon caused by noise, but also improves the anti-noise ability and edge detection ability.

Figure 10 show that the confusion matrixes and ROC curves of the proposed method under 10% testing data of the Pavia University dataset. In this paper, we use the AUC value to mark the quality of the classifier, which is the size of the area under the ROC curve. The higher the AUC value is, the better the classification accuracy is. The area or AUC values in the figure are rounded.

Tables 6 and 7 report the accuracies of all classes with the OAs, Kappa coefficients for hyperspectral oil spill detection classification. As shown in Tables 6 and 7, the proposed method achieves the best classification results on both oil spill datasets compared with other classification methods.
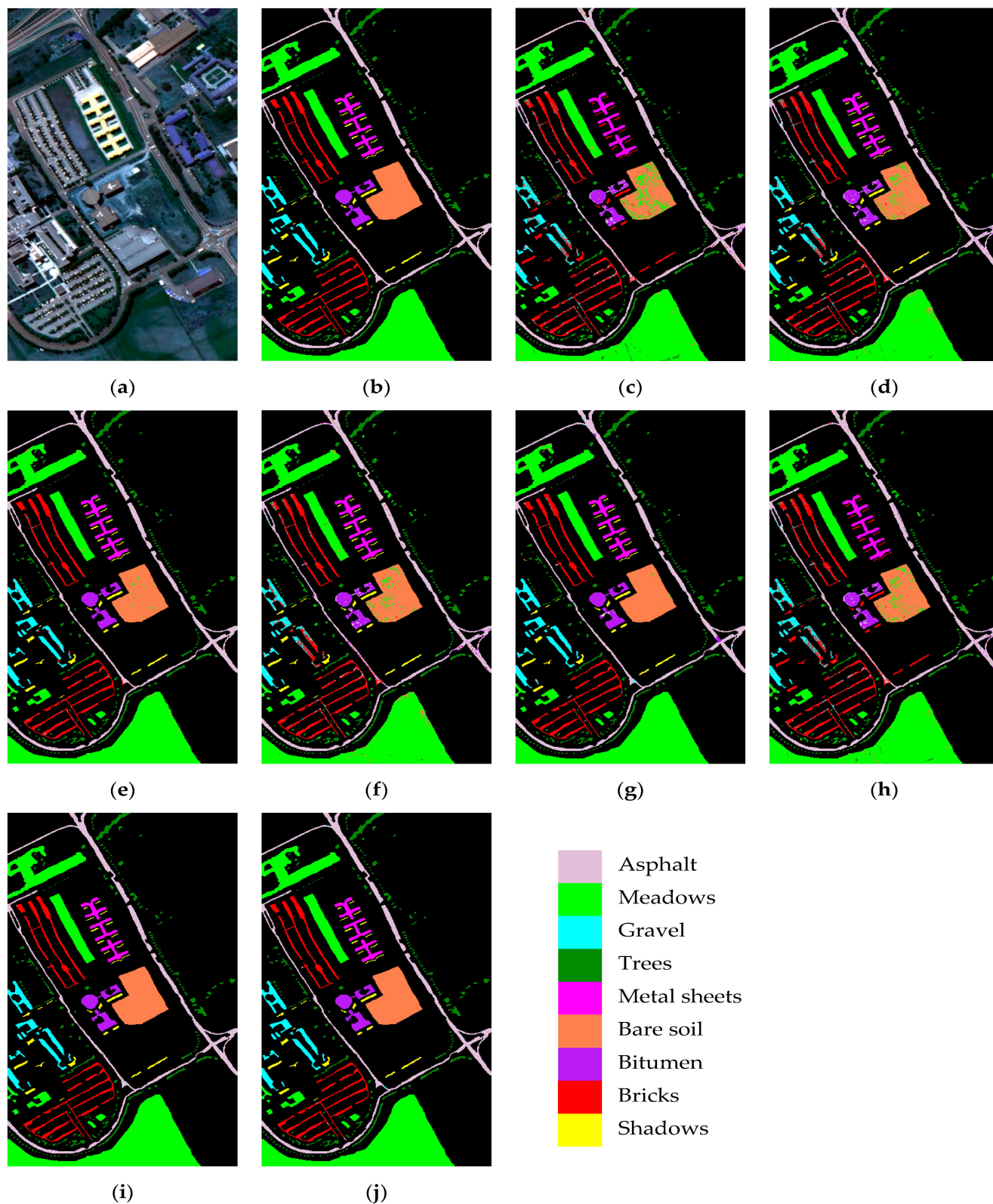
FIGURE 7. Hyperspectral image classification results of the Pavia University Dataset. (a) False-color image. (b) Ground truth. (c) Adaboost. (d) RF. (e) KNN. (f) SVM. (g) LeNet-5. (h) 1D-CNN. (i) 2D-CNN. (j) CNN$_{spe+spa}$.
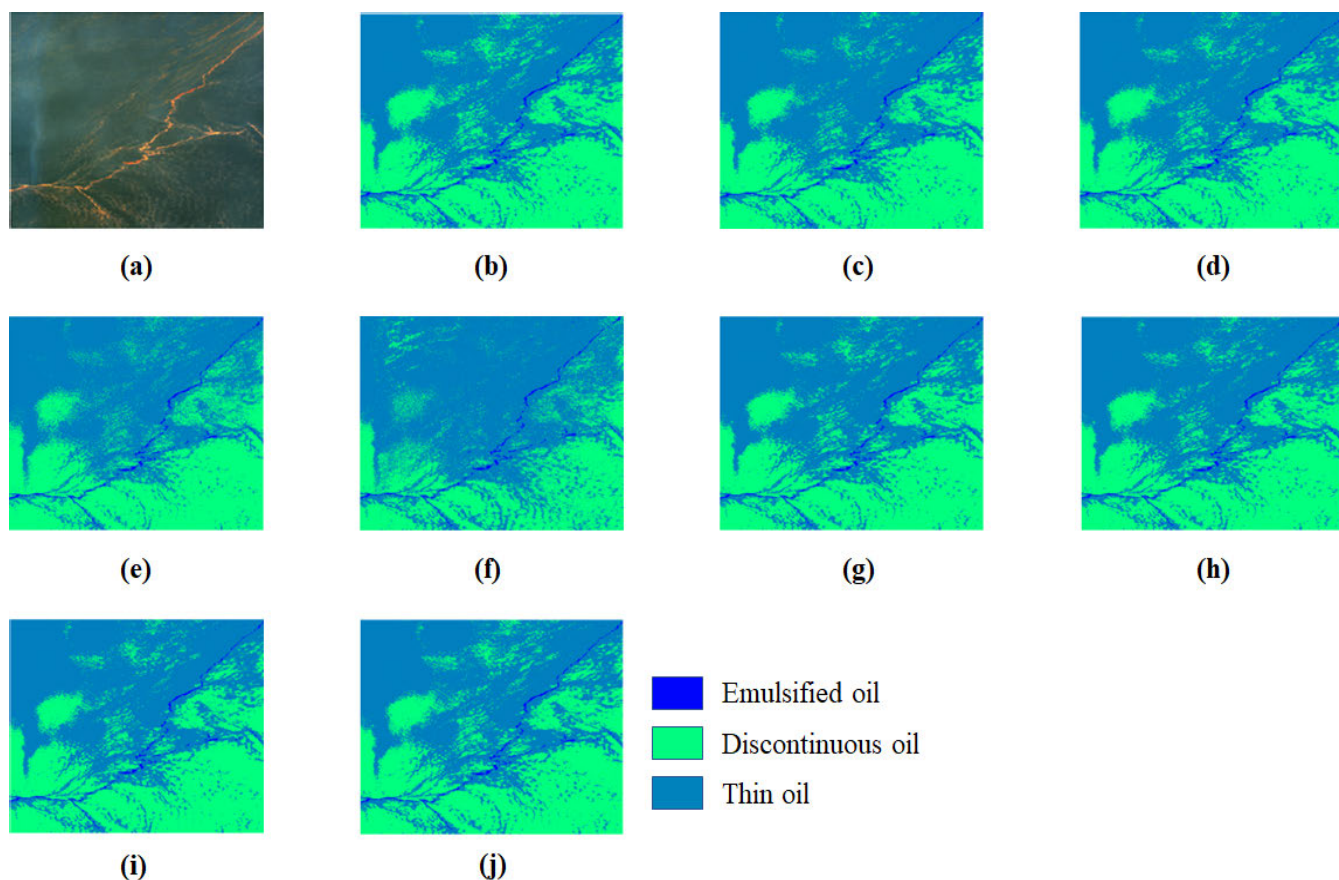
FIGURE 8. Hyperspectral image classification results of the oil spill area 1. (a) False-color image. (b) Ground truth. (c) Adaboost. (d) RF. (e) KNN. (f) SVM. (g) LeNet-5. (h) 1D-CNN. (i) 2D-CNN. (j) CNN$_{spe+spa}$.

TABLE 6. Classification results of different methods for oil spill area 1.

No.	Class	Adaboost	RF	KNN	SVM	Lenet-5	1D-CNN	2D-CNN	CNN$_{spe+spa}$
1	Thin oil	94.56	98.56	98.43	87.01	84.53	89.67	98.38	98.71
2	Discontinuous oil	89.23	92.97	99.66	84.91	88.45	96.64	98.11	98.87
3	Emulsified oil	94.31	96.80	87.84	70.68	85.34	98.51	84.58	99.61
	OA	91.56	95.42	98.03	85.72	86.73	93.64	98.13	99.85
	(%)	±1.24	±0.69	±0.17	±3.35	±1.45	±1.68	±1.87	±0.07
	Kappa	83.27	90.92	96.07	71.56	73.44	87.19	96.26	99.70
	(%)	±2.36	±2.12	±0.43	±3.54	±1.63	±0.96	±1.79	±0.15
	Test.Time(s)	127.25	134.82	149.77	123.30	149.13	205.21	377.95	427.30
	Train.Time(s)	45.68	65.34	67.36	54.65	73.21	102.82	160.53	196.05

As shown in Table 6, SVM yielded poor accuracies in the "Thin oil", "Thick oil" classes, which are 70.68%, 84.91%, respectively. This is caused by "foreign bodies with spectrum", means that their similarity of spectral curves, which makes it difficult for models to distinguish them.

As shown in Table 7, CNN$_{spe+spa}$ achieved the best OA, was 7.12%, 3.81%, 1.72%, 10.85%, 11.74%, 4.60% higher than that of Adaboost, RF, KNN, SVM, LeNet-5, 1D-CNN. It serves to show that the proposed SSFE has a relatively stable and equilibrium classification accuracies for each category under strong spatial domain relationships and obtained the maximum OA value (99.85%) and Kappa value (99.70%).

It can be noticed that the proposed SSFE method can capture subtle information and is indispensable and advantageous for the proposed method. Furthermore, according to the table, the proposed SSFE achieves the expected result of classification accuracy on two oil spill datasets. There are some shortcomings among models, on account of the actual spectra of thin oil and seawater are not easily distinguishable, this results in misclassification. The classification results show that the proposed method is useful for oil spill classification. The false alarm rate have been reduced.

Figure 11 and Figure 12 are the confusion matrixes and ROC curves of the proposed model under 10% testing data
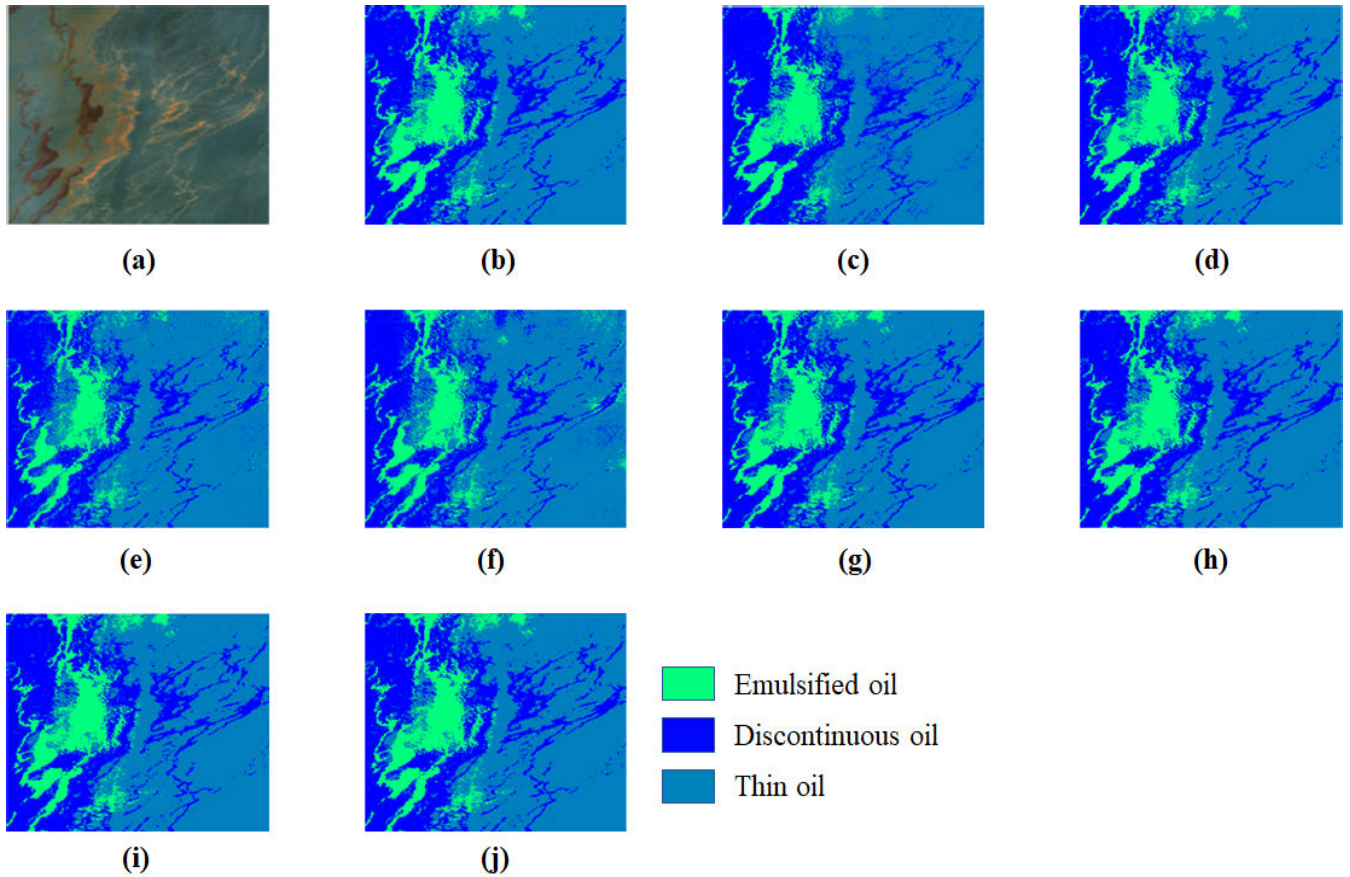
FIGURE 9. Hyperspectral image classification results of the oil spill area 2. (a) False-color image. (b) Ground truth. (c) Adaboost. (d) RF. (e) KNN. (f) SVM. (g) LeNet-5. (h) 1D-CNN. (i) 2D-CNN. (j) $CNN_{spe+spa}$.
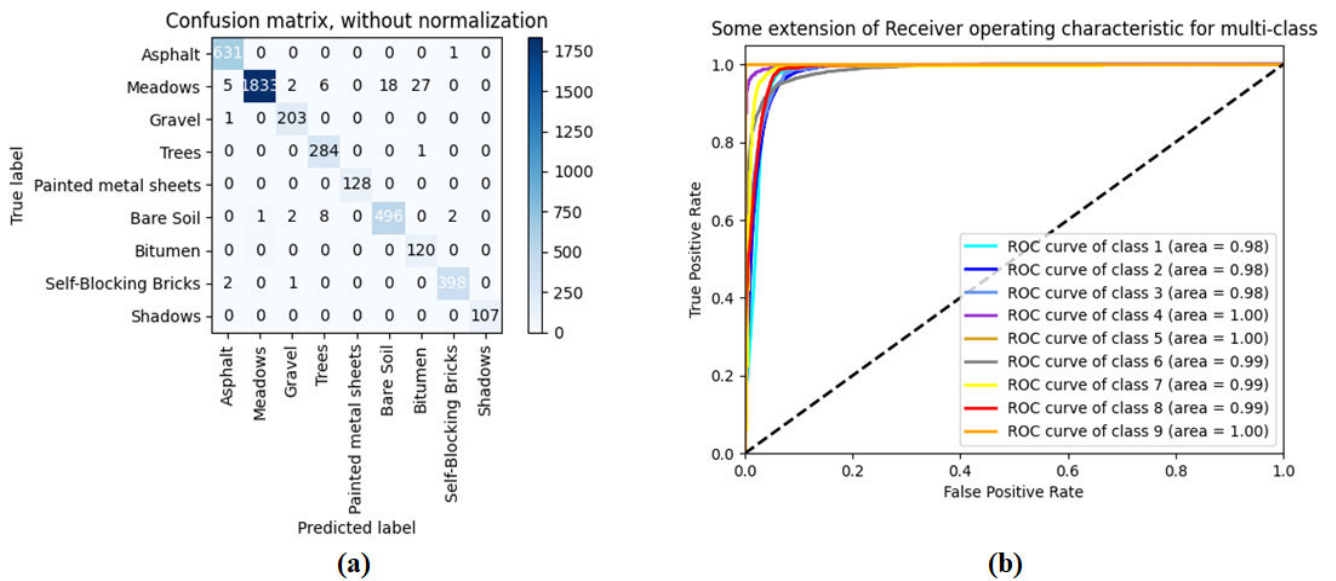
FIGURE 10. Confusion matrix and ROC curve under Pavia University 10% testing data: (a) Confusion matrix (b) ROC curve.

of the oil spill area 1 and the oil spill area 2. In the confusion matrix, each column value represents the predicted value, and each row value shows the actual category and the diagonal value denotes the number of corrected classifications. The area or AUC values in the figure are rounded. It can be seen that the classification results of each category is ideal.

FIGURE 11. Confusion matrix and ROC curve under oil spill area 1 10% testing data: (a) Confusion matrix (b) ROC curve.

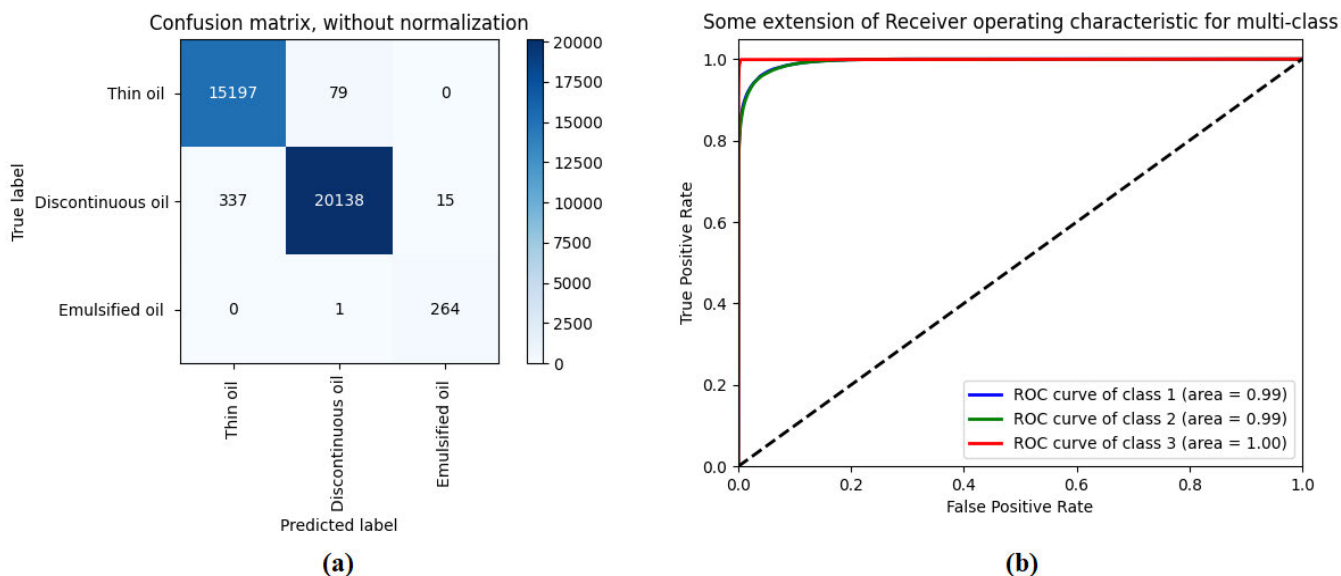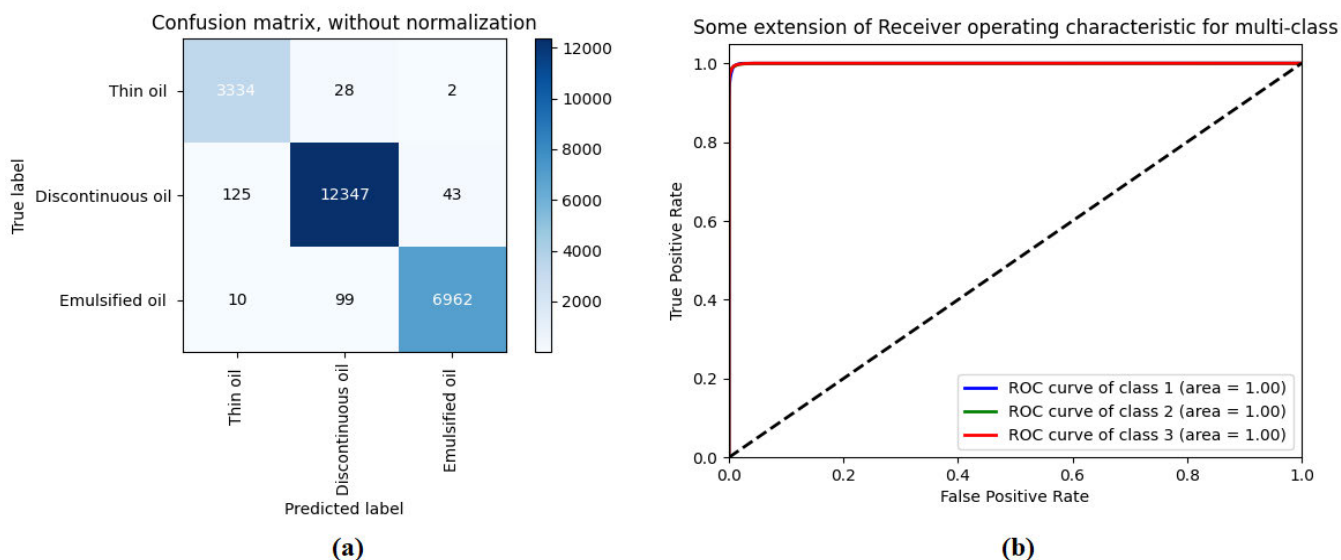**FIGURE 12.** Confusion matrix and ROC curve under oil spill area 2 10% testing data: (a) Confusion matrix (b) ROC curve.

TABLE 7. Classification results of different methods for oil spill area 2.

No.	Class	Adaboost	RF	KNN	SVM	Lenet-5	1D-CNN	2D-CNN	CNN$_{spe+spa}$
1	Thin oil	97.29	97.38	94.09	77.90	77.15	90.59	91.34	99.60
2	Discontinuous oil	96.43	97.30	98.73	94.62	91.77	97.07	98.04	99.90
3	Emulsified oi	93.64	93.71	98.30	75.79	83.06	95.79	94.86	99.82
	OA	95.70	96.21	97.90	86.34	85.42	95.71	96.07	99.86
	(%)	±0.69	±0.82	±1.36	±2.67	±2.75	±1.88	±2.64	±0.07
	Kappa	92.75	93.59	96.42	76.91	74.66	92.70	93.28	99.76
	(%)	±0.80	±0.93	±1.78	±1.62	±2.53	±0.26	±1.76	±0.12
	Test.Time(s)	135.85	176.43	197.26	142.34	166.57	207.62	393.34	467.51
	Train.Time(s)	63.26	85.17	91.70	76.59	84.97	109.63	191.26	216.29

Table 5 lists classification index diagram under multiclass conditions, Table 6 and 7 lists the precision, recall rate, and F1-score of each category, as well as the macro-averaged and weighted-averaged quantities for the proposed method

TABLE 8. Classification index diagram under multiclass conditions.

True condition	Predicted condition	
	Positive condition	Negative condition
Positive condition	True positive (TP)	False negative (FN)
Negative condition	False negative (FP)	True negative (TN)

TABLE 9. The precision, recall, and F1-score for the Pavia University dataset.

No.	Class	Precision	Recall	F1-Score
1	Asphalt	99.64	98.32	99.48
2	Meadows	99.72	98.48	99.85
3	Gravel	99.00	97.79	99.44
4	Trees	98.35	99.71	98.53
5	Metal Sheets	100.00	100.00	100.00
6	Bare Soil	100.00	99.28	100.00
7	Bitumen	100.00	99.42	99.71
8	Bricks	99.72	98.52	99.12
9	Shadows	98.46	100.00	98.17
	macro-averaged	99.43	99.30	99.37
	weighted-averaged	99.60	99.59	99.59

upon the three datasets. In the macro-averaged, the index value is first calculated for each class, and then the arithmetic average is calculated for all classes. Their formulas are given as follows. As can be seen from the table, there are three indicators of the thin oil film on the low side, implying high probability of misclassification, which eventually indicates that the detection ability of the algorithm for the thin oil film needs to be further improved. Nevertheless, the superior precision, recall rate, and F1-score still indicate that the classifier is effective for hyperspectral oil spill detection.

$$Accuracy_{macro\_avg}$$
$$= \sum_{i=1}^{N} \frac{1}{N} \times \frac{TP_i + TN_i}{TP_i + TN_i + FP_i + FN_i} \qquad (4)$$

$$Accuracy_{weight\_avg}$$
$$= \sum_{i=1}^{N} \frac{TP_i + TN_i}{\sum_{j=1}^{N} TP_i + FN_i} \times \frac{Accuracy_{macro\_avg}}{\sum_{i=1}^{N} \frac{1}{N}} \qquad (5)$$

where TP represents positive classes are predicted to be positive, true is 0, and prediction is 0, TN represents negative classes are predicted to be negative, true is 1, and prediction is 1, FN represents positive samples that are predicted to be negative by the model, and FP denote negative samples that are predicted to be positive by the model. i represents the ith category and N represents the total number of categories.

IV. DISCUSSIONS
In this paper, a fusion model of spectral and spatial features for HRSI classification based on CNNs is constructed. The network is then trained by training samples. The optimal classification results are obtained as training samples. Firstly,

the University of Pavia experimental results of hyperspectral data show that the proposed model can improve the classification accuracy of hyperspectral remote sensing images. The classification accuracy of "Bare Soil" class in various models is very unstable, this is because the classification accuracy of this class on 2D-CNN is high, it has rich spatial information, spectral information feature is weaker than spatial information feature, and the proposed model uses more spectral information than other models, and finally the classification of this class is accurate degree is reduced. Because different components absorb different spectra, spectral information can fully reflect the physical structure and chemical information inside the sample, and has advantages in the accurate identification and fine classification of different vegetation and minerals. However, for "Gravel" and other objects with prominent texture characteristics, the classification effect of high spectral information is not so good. "Bitumen", "Gravel" and other vegetation have rich one-dimensional spectral information, so the classification accuracy is opposite to that of "Bare Soil", and the classification accuracy on 2D-CNN is lower than that on 1D-CNN. The classification accuracy has been greatly improved.

This can be seen from the comparison results of different methods, SVM and Lenet-5 does not recognize well spectral characteristics similar to thin and thick oil film, seawater. For 2D-CNN, due to the small number of samples selected for thick oil film, there is less spatial information that can be used for training analysis on oil spill area 1, so the classification accuracy is lower than 1D-CNN. Although the AVIRIS images of the experimental areas is affected by solar flare and seawater composition, the seawater environment in the sea polluted by oil film is uneven. However, through

TABLE 10. The precision, recall, and F1-score for oil spill area 1 and oil spill area 2.

	No.	Class	Precision	Recall	F1-Score
oil spill area 1	1	Thin oil	99.99	98.71	99.85
	2	Discontinuous oil	99.76	98.97	99.87
	3	Emulsified oil	98.63	99.61	98.97
	macro-averaged		99.46	99.60	99.60
	weighted-averaged		99.85	99.85	99.85
oil spill area 2	1	Thin oil	99.60	99.60	99.60
	2	Discontinuous oil	99.85	99.90	99.90
	3	Emulsified oi	99.90	99.92	98.92
	macro-averaged		99.82	99.82	99.81
	weighted-averaged		99.86	99.86	99.86

training of divided oil film and sea water sample, oil film under uneven sea water environment can still be identified and the "false target" of oil film caused by uneven sea water condition can be eliminated. Although the proposed SSFE method costs huge time to train the network, it can also be showed that the classification accuracy is still very high. Due to the large number of test samples, the computational complexity and time are also larger. For training numbers of the Pavia University dataset, it costs 143.66s, its image size is $610 \times 340 \times 103$. For oil spill area 1 dataset, it costs 196.05s, its image size is $526 \times 685 \times 192$. The oil spill area 2 dataset has the largest time cost 216.29s, its image size is $425 \times 540 \times 192$. The difference between the test and the training sample makes the time differences.

A suitable method can reduce the number of free parameters of the network and make the generalization ability of the trained model stronger, which is very important for further feature extraction and classification. Due to the impact of "same thing different spectrum", "same spectrum foreign body", and the uncertainty of the marine surface environment, the spectral curve contours of oil film of different thickness is slightly differences, and it's not easy to tell the exact difference. Using only Spectral characteristics alone is often insufficient to accurately extract target object. Instead, the texture information of the oil spill and seawater exerts a significant difference and the boundary line between them is evident, judging from the oil spill RGB image.

V. CONCLUSION
In this paper, we have proposed SSFE method to extract the spectral-spatial based deep features. The major contributions of this paper are summarized as follows.

1) Compared with traditional spectral-spatial classification framework which are separated from each other. We use a spectral 1D-CNN and spatial 2D-CNN model with high spectral resolution and band continuity in the spectral region and a small neighborhood size in the spatial region to extract the unified features of HRSI.

2) In order to deal with data imbalance or classification effect is not ideal. We add a class_weight to each category in the training set during oil data sets model training. The OA can be improved for oil datasets with the proposed method.

Although we utilize the proposed SSFE method as the spectral and spatial feature extractors, other deep learning networks or machine learning model can also be imported in our model. It was worth to be investigated in the future work. Between the spectral loss and the spatial loss will also be discussed in our future work. Due to the different spectral and spatial features in the selected scenes and samples, the selection and learning of appropriate weighting factors are also worthy of study for hyperspectral classification. CNN is topical issues in computer realm. In recent years, a number of different models have emerged, and they can be also used for the proposed CNN model. The proposed method can be combined with post-processing of data classification to strengthen mirroring capability.

REFERENCES
[1] P. Li, Q. Cai, W. Lin, B. Chen, and B. Zhang, "Offshore oil spill response practices and emerging challenges," *Mar. Pollut. Bull.*, vol. 110, no. 1, pp. 6–27, Sep. 2016.
[2] S. E. Chang, J. Stone, K. Demes, and M. Piscitelli, "Consequences of oil spills: A review and framework for informing planning," *Ecology Soc.*, vol. 19, no. 2, p. 26, 2014.
[3] J. Chen, W. Zhang, Z. Wan, S. Li, T. Huang, and Y. Fei, "Oil spills from global tankers: Status review and future governance," *J. Cleaner Prod.*, vol. 227, pp. 20–32, Aug. 2019.
[4] Q. Tong, Y. Xue, and L. Zhang, "Progress in hyperspectral remote sensing science and technology in China over the past three decades," *IEEE J. Sel. Topics Appl. Earth Observ. Remote Sens.*, vol. 7, no. 1, pp. 70–91, Jan. 2014.
[5] S. Zeng, Z. Wang, C. Gao, Z. Kang, and D. Feng, "Hyperspectral image classification with global–local discriminant analysis and spatial–spectral context," *IEEE J. Sel. Topics Appl. Earth Observ. Remote Sens.*, vol. 11, no. 12, pp. 5005–5018, Dec. 2019.
[6] J. Liu, X. Guo, and Y. Liu, "Hyperspectral remote sensing image feature extraction based on spectral clustering and subclass discriminant analysis," *Remote Sens. Lett.*, vol. 11, no. 2, pp. 166–175, Feb. 2020.
[7] U. Sakarya, "Hyperspectral dimension reduction using global and local information based linear discriminant analysis," *ISPRS Ann. Photogramm., Remote Sens. Spatial Inf. Sci.*, vols. II–7, pp. 61–66, Sep. 2014.
[8] X. Cui, K. Zheng, L. Gao, B. Zhang, D. Yang, and J. Ren, "Multi-scale spatial–spectral convolutional network with image-based framework for hyperspectral imagery classification," *Remote Sens.*, vol. 11, no. 19, p. 2220, Sep. 2019.
[9] J. Yang and J. Qian, "Hyperspectral image classification via multiscale joint collaborative representation with locally adaptive dictionary," *IEEE Geosci. Remote Sens. Lett.*, vol. 15, no. 1, pp. 112–116, Jan. 2017.
[10] L. Fang, N. He, S. Li, A. J. Plaza, and J. Plaza, "A new spatial–spectral feature extraction method for hyperspectral images using local covariance matrix representation," *IEEE Trans. Geosci. Remote Sens.*, vol. 56, no. 6, pp. 3534–3546, Jun. 2018.

[11] S. Tong, X. Liu, Q. Chen, Z. Zhang, and G. Xie, "Multi-feature based ocean oil spill detection for polarimetric SAR data using random forest and the self-similarity parameter," *Remote Sens.*, vol. 11, no. 4, p. 451, Feb. 2019.

[12] S. Delalieux, B. Somers, and B. Haest, "Heathland conservation status mapping through integration of hyperspectral mixture analysis and decision tree classifier," *Remote Sens. Environment.*, vol. 126, pp. 222–231, Nov. 2012.

[13] Y. Zhong and L. Zhang, "An adaptive artificial immune network for supervised classification of multi-/hyperspectral remote sensing imagery," *IEEE Trans. Geosci. Remote Sens.*, vol. 50, no. 3, pp. 894–909, Mar. 2012.

[14] J. Peng, Y. Zhou, and C. L. P. Chen, "Region-kernel-based support vector machines for hyperspectral image classification," *IEEE Trans. Geosci. Remote Sens.*, vol. 53, no. 9, pp. 4810–4824, Sep. 2015.

[15] Z. Jiao, G. Jia, and Y. Cai, "A new approach to oil spill detection that combines deep learning with unmanned aerial vehicles," *Comput. Ind. Eng.*, vol. 135, pp. 1300–1311, Sep. 2019.

[16] X. Yaohua and M. Xudong, "A SAR oil spill image recognition method based on DenseNet convolutional neural network," in *Proc. Int. Conf. Robots Intell. Syst. (ICRIS)*, Jun. 2019, pp. 78–81.

[17] B. Liu, Q. Zhang, Y. Li, W. Chang, and M. Zhou, "Spatial–spectral jointed stacked auto-encoder-based deep learning for oil slick extraction from hyperspectral images," *J. Indian Soc. Remote Sens.*, vol. 47, no. 12, pp. 1989–1997, Dec. 2019.

[18] G. Chen, Y. Li, G. Sun, and Y. Zhang, "Application of deep networks to oil spill detection using polarimetric synthetic aperture radar images," *Appl. Sci.*, vol. 7, no. 10, p. 968, Sep. 2017.

[19] H. Guo, D. Wu, and J. An, "Discrimination of oil slicks and lookalikes in polarimetric SAR images using CNN," *Sensors*, vol. 17, no. 8, p. 1837, Aug. 2017.

[20] Y. Chen, Y. Li, and J. Wang, "An end-to-end oil-spill monitoring method for multisensory satellite images based on deep semantic segmentation," *Sensors*, vol. 20, no. 3, p. 725, Jan. 2020.

[21] M. Krestenitis, G. Orfanidis, K. Ioannidis, K. Avgerinakis, S. Vrochidis, and I. Kompatsiaris, "Oil spill identification from satellite images using deep neural networks," *Remote Sens.*, vol. 11, no. 15, p. 1762, Jul. 2019.

[22] J. Zhang, H. Feng, Q. Luo, Y. Li, J. Wei, and J. Li, "Oil spill detection in quad-polarimetric SAR images using an advanced convolutional neural network based on superpixel model," *Remote Sens.*, vol. 12, no. 6, p. 944, Mar. 2020.

[23] H. Guo, G. Wei, and J. An, "Dark spot detection in SAR images of oil spill using SegNet," *Appl. Sci.*, vol. 8, no. 12, p. 2670, Dec. 2018.

[24] A.-J. Gallego, P. Gil, A. Pertusa, and R. B. Fisher, "Semantic segmentation of SLAR imagery with convolutional LSTM selectional autoencoders," *Remote Sens.*, vol. 11, no. 12, p. 1402, Jun. 2019.

[25] G. Orfanidis, K. Ioannidis, K. Avgerinakis, S. Vrochidis, and I. Kompatsiaris, "A deep neural network for oil spill semantic segmentation in SAR images," in *Proc. 25th IEEE Int. Conf. Image Process. (ICIP)*, Oct. 2018, pp. 3773–3777.

[26] D. Cantorna, C. Dafonte, A. Iglesias, and B. Arcay, "Oil spill segmentation in SAR images using convolutional neural networks. A comparative analysis with clustering and logistic regression algorithms," *Appl. Soft Comput.*, vol. 84, Nov. 2019, Art. no. 105716.

[27] Y. LeCun, Y. Bengio, and G. Hinton, "Deep learning," *Nature*, vol. 521, pp. 436–444, Feb. 2015.

[28] R. Al-Ruzouq, M. B. A. Gibril, A. Shanableh, A. Kais, O. Hamed, S. Al-Mansoori, and M. A. Khalil, "Sensors, features, and machine learning for oil spill detection and monitoring: A review," *Remote Sens.*, vol. 12, no. 20, p. 3338, Oct. 2020.

[29] H. Guo, H. Bai, Y. Zhou, and W. Li, "DF-SSD: A deep convolutional neural network-based embedded lightweight object detection frame work for remote sensing imagery," *J. Appl. Remote Sens.*, vol. 14, no. 1, 2020, Art. no. 014521.

[30] G. A. Fricker, J. D. Ventura, J. A. Wolf, M. P. North, F. W. Davis, and J. Franklin, "A convolutional neural network classifier identifies tree species in mixed-conifer forest from hyperspectral imagery," *Remote Sens.*, vol. 11, no. 19, p. 2326, Oct. 2019.

[31] S. Chen, M. Jin, and J. Ding, "Hyperspectral remote sensing image classification based on decomposed three-dimensional convolutional neural network," *Multimedia Tools Appl.*, vol. 80, pp. 1859–1882, Sep. 2021.

[32] M. Sabokrou, M. Fayyaz, M. Fathy, and R. Klette, "Deep-cascade: Cascading 3D deep neural networks for fast anomaly detection and localization in crowded scenes," *IEEE Trans. Image Process.*, vol. 26, no. 4, pp. 1992–2004, Apr. 2017.

[33] S. A. Sakaci and O. Urhan, "Spectral-spatial classification of hyperspectral imagery with convolutional neural network," in *Proc. Innov. Intell. Syst. Appl. Conf. (ASYU)*, Oct. 2020, pp. 1–4.

[34] J. Leng, T. Li, G. Bai, Q. Dong, and H. Dong, "Cube-CNN-SVM: A novel hyperspectral image classification method," in *Proc. IEEE 28th Int. Conf. Tools Artif. Intell. (ICTAI)*, Nov. 2016, pp. 1027–1034.

[35] Q. Xu, Y. Xiao, D. Wang, and B. Luo, "CSA-MSO3DCNN: Multiscale octave 3D CNN with channel and spatial attention for hyperspectral image classification," *Remote Sens.*, vol. 12, no. 1, p. 188, Jan. 2020.

[36] S. K. Roy, G. Krishna, S. R. Dubey, and B. B. Chaudhuri, "HybridSN: Exploring 3-D-2-D CNN feature hierarchy for hyperspectral image classification," *IEEE Geosci. Remote Sens. Lett.*, vol. 17, no. 2, pp. 277–281, Jun. 2020.

[37] J. Zhang, F. Wei, F. Feng, and C. Wang, "Spatial–spectral feature refinement for hyperspectral image classification based on attention-dense 3D-2D-CNN," *Sensors*, vol. 20, no. 18, p. 5191, Sep. 2020.

[38] M. Han, R. Cong, X. Li, H. Fu, and J. Lei, "Joint spatial–spectral hyperspectral image classification based on convolutional neural network," *Pattern Recognit. Lett.*, vol. 130, pp. 38–45, Feb. 2020.

[39] B. Liu, Y. Li, G. Li, and A. Liu, "A spectral feature based convolutional neural network for classification of sea surface oil spill," *ISPRS Int. J. Geo-Inf.*, vol. 8, no. 4, p. 160, Mar. 2019.

[40] X. Zhu, Y. Li, Q. Zhang, and B. Liu, "Oil film classification using deep learning-based hyperspectral remote sensing technology," *ISPRS Int. J. Geo-Inf.*, vol. 8, no. 4, p. 181, Apr. 2019.

[41] J. Schmidhuber, "Deep learning in neural networks: An overview," *Neural Netw.*, vol. 61, pp. 85–117, Oct. 2015.

[42] Y. Xu, L. Zhang, B. Du, and F. Zhang, "Spectral-spatial unified networks for hyperspectral image classification," *IEEE Trans. Geosci. Remote Sens.*, vol. 56, no. 10, pp. 5893–5909, Oct. 2018.

[43] G. Hinton, N. Srivastava, A. Krizhevsky, R. R. Salakhutdinov, and I. Sutskever, "Improving neural networks by preventing co-adaptation of feature detectors," *Comput. Sci.*, vol. 3, no. 4, pp. 212–223, Jul. 2012.

[44] D. P. Kinma and J. L. Ba, "Adam: A method for stochastic optimization," in *Proc. Int. Conf. Learn. Represent.*, San Diego, CA, USA, 2014, pp. 1–13.

[45] M. Seydgar, A. A. Naeini, M. Zhang, W. Li, and M. Satari, "3-D convolution-recurrent networks for spectral-spatial classification of hyperspectral images," *Remote Sens.*, vol. 11, no. 7, p. 883, Jan. 2019.

[46] F. Mohammadimanesh, B. Salehi, M. Mahdianpari, E. Gill, and M. Molinier, "A new fully convolutional neural network for semantic segmentation of polarimetric SAR imagery in complex land cover ecosystem," *ISPRS J. Photogramm. Remote Sens.*, vol. 151, pp. 223–236, May 2019.

[47] G. An, Z. Jiang, X. Cao, Y. Liang, Y. Zhao, Z. Li, W. Dong, and H. Sun, "Short-term wind power prediction based on particle swarm optimization-extreme learning machine model combined with AdaBoost algorithm," *IEEE Access*, vol. 9, pp. 94040–94052, 2021.

[48] C. Zhang, X. Yue, R. Wang, N. Li, and Y. Ding, "Study on traffic sign recognition by optimized LeNet-5 algorithm," *Int. J. Pattern Recognit. Artif. Intell.*, vol. 34, no. 1, Jan. 2020, Art. no. 2055003.

[49] J. Rala Cordeiro, A. Raimundo, O. Postolache, and P. Sebastião, "Neural architecture search for 1D CNNs—Different approaches tests and measurements," *Sensors*, vol. 21, no. 23, p. 7990, Nov. 2021.

[50] I. Amerini, C. Li, and R. Caldelli, "Social network identification through image classification with CNN," *IEEE Access*, vol. 7, pp. 35264–35273, 2019.

TAO HU was born in Changzhi, Shanxi, China, in 1996. He received the B.S. degree in physics from the Hubei University of Arts and Sciences, China, in 2020. He is currently pursuing the Ph.D. degree in optical engineering with the Changchun Institute of Optics, Fine Mechanics and Physics, Chinese Academy of Sciences, Changchun, China. His current research interests include application of spectra, hyper-spectral remote sensing, and application of remote sensing in oil.

JING YUAN was born in Changchun, Jilin, China, in 1993. She received the B.S. degree in optical information science and technology from Jilin University, China, in 2016. She is currently pursuing the Ph.D. degree in optical engineering with the Changchun Institute of Optics, Fine Mechanics and Physics, Chinese Academy of Sciences, Changchun. Her current research interests include application of spectra, hyper-spectral remote sensing, and application of remote sensing in soil.

XIAODONG WANG was born in Baishan, Jilin, China, in 1970. He received the M.S. degree in engineering and the Ph.D. degree from the Changchun Institute of Optics, Fine Mechanics and Physics, Chinese Academy of Sciences, Changchun, China, in 1998 and 2003, respectively.

Since 2003, he has been the Director of the Changchun Institute of Optics, Fine Mechanics and Physics, Chinese Academy of Sciences. His research interests include imaging technology and information processing of space optical remote sensing instrument.

CHANGXIANG YAN was born in Honghu, Hubei, China, in 1973. He received the M.S. degree in engineering from Zhejiang University, Zhejiang, China, in 1998, and the Ph.D. degree from the Changchun Institute of Optics, Fine Mechanics and Physics, Chinese Academy of Sciences, Changchun, China, in 2001.

Since 2010, he has been the Director of the Space Optics Laboratory, Changchun Institute of Optics, Fine Mechanics and Physics, Chinese Academy of Sciences. His research interests include opto-mechatronics technology for space optical remote sensing instruments, multispectral and hyper-spectral spatial remote sensing imaging, polarization detection, and space surveillance.

XUEPING JU was born in Songyuan, Jilin, China, in 1991. He received the B.S. degree in control technology and instruments from Tianjin University, China, in 2014, and the Ph.D. degree in optical engineering from the Changchun Institute of Optics, Fine Mechanics and Physics, Chinese Academy of Sciences, Changchun, China, in 2019. His current research interest includes polarization calibration.

● ● ●